 cmes, vol.5, no.4, pp.295-317, 2004

Development of New Algorithms for High Frequency Electromagnetic Scattering

E. Bleszynski[1], M. Bleszynski[1], and T. Jaroszewicz[1]

Abstract: We describe elements of our current work on the development of new methods for high frequency electromagnetic scattering, based on the wavefront (WF) representation of propagating fields and on the asymptotic but rigorous solution of integral equations for surface currents. In the wavefront evolution technique, surfaces of constant phase are constructed and treated not merely as collections of independent rays, but as well defined geometrical objects endowed with the full connectivity information. Hence, a precise determination of shadow and reflection boundaries, a construction of (multiply) diffracted wavefronts, a dynamic adjustment of the number of rays, an approximately constant ray-ray distance, and an accurate evaluation of fields on the wavefronts by means of interpolation between the neighboring rays are possible. As such, the wavefront evolution approach constitutes a significant improvement over conventional ray tracing methods. An essential element of the asymptotic, high frequency integral-equation (HFIE) method is the solution Ansatz, i.e., the representation of the current as a sum of known rapidly oscillating functions multiplied by unknown smooth functions varying slowly over the distance of a wavelength. While the form of the Ansatz is relatively straightforward for simple geometries, it becomes quite complicated for complex objects. We propose a general numerical procedure for the Ansatz construction which is based on determination of the rapidly oscillating components of the Ansatz from surface fields generated by a sequence of wavefronts corresponding to physically relevant multiple reflection and diffraction processes. Since both the Ansatz construction and the asymptotic integral equation approach will require the same discretization, determined not by the wavelength but by the geometrical complexity of the scatterer and the desired accuracy of the asymptotic expansion, the number of unknowns in the approach will be frequency independent. We also present results of our analysis of the ability and accuracy of the WF and HFIE approaches in capturing such important physical phenomena as multiple scattering, diffraction, surface waves and cross-polarization effects.

keyword: Computational electromagnetics, wavefronts, high frequency integral equations.

1 Introduction

Problems involving ground combat vehicles in the frequency range up to 100 GHz require development of new methods. With the recent advances in the state-of-the-art matrix compression techniques based on Fast Multipole Method (FMM) [Coifman, Rokhlin and Wandzura (1993)] and Fast Fourier Transform (FFT)-type (AIM) algorithms [Bleszynski, Bleszynski and Jaroszewicz (1996), Bruno and Kunyansky (2001)], it is possible to carry out calculations involving realistic military vehicles whose geometry representations contain several (1 – 20) million unknowns. For example, radar signature calculations for a fairly representative model of a ground combat vehicle at 2 GHz, containing, depending on the level of details, about 1 million unknowns, would require approximately one day on 32 processor Origin 2000. Calculations with larger number of unknowns, although possible, become gradually impractical; calculations for the same vehicle at 100 GHz would require about 2.5 billion unknowns. In addition, more realistic simulations of a ground scene call for inclusion of high clutter environments (ground, trees, etc.), and multi-look angle, multi-frequency solutions for radar processing.

New faster and accurate techniques need to be developed capable of capturing accurately all relevant physical phenomena contributing to radar signatures, such as multiple reflection, surface waves, and (multiple) edge diffraction. These my be either approximate methods involving hybridization of high frequency (HF) and low frequency (LF) solutions, or new asymptotic high frequency methods.

The conventional hybrid methods are usually based on

[1] Monopole Research, Thousand Oaks, CA 91360, USA

partitioning of the geometry into domains, and applying different solution methods (conventional method of moments (MoM), FFT and FFM-based compression schemes, HF methods) to individual domains. A challenging problem in this approach is reducing the computational complexity of coupling between the domains while maintaining accuracy of the solution. Significant benefits stemming from the development of hybrid approaches combined with the improvement of LF impedance matrix compression based modules are as follows:

(i) They allow us to solve, with different degrees of accuracy, various practical problems, before new fully developed high frequency solvers become available.

(ii) They allow us to validate accuracy of various coupling schemes.

(iii) They form a framework for the validation and hence acceleration of the development of new HF approaches.

The first approach we discuss in this paper is the wavefront (WF) evolution method. WF evolution method is a relatively new approach in problems of electromagnetic propagation. It has been largely followed in the context of geophysical applications (see, e.g., [Vinje, Iversen, Astebol and Gjöystdal (1996a), Vinje, Iversen, Astebol and Gjöystdal (1996b)]). Alternative, "Eulerian" methods [Steinhoff, Fan and Wang (2000), Ruuth, Merriman and Osher (2000), Osher and Fedkiw (2002)], have been recently advanced describing propagation of scalar waves. We also note, that recent improvements of the Eulerian wavefront method which result in, e.g., improved stability of the solutions in the presence of multiple reflections, are presented in [Cheng, Kang, Osher, Shim, and Tsai (2004)]

In the WF evolution technique, surfaces of constant phase are constructed and treated not merely as collections of independent rays (or "ray tubes"), but as well defined geometrical objects endowed with the full connectivity information. This information allows a precise determination of shadow and reflection boundaries, a construction of (multiply) diffracted wavefronts, and an accurate evaluation of fields on the wavefronts by means of interpolation between the neighboring rays. In this way, the wavefront evolution technique constitutes a significant improvement over conventional ray tracing methods. It also allows for adjustments in the number of rays in situations when the WF expands or shrinks, and maintains in this way approximately constant ray-ray distances. The last feature improves the efficiency of the WF method compared to conventional ray shooting and bouncing methods by eliminating the need of creating very dense sets of incident rays.

Our developments in the area of WF methods provide a major extension of the previous work by including ***diffraction*** effects. We construct diffracted wavefronts by geometrical methods. Subsequently, diffracted fields obtained from the Geometrical Theory of Diffraction (GTD) or Uniform Geometrical Theory of Diffraction (UTD) (see, e.g., [Keller (1962), Kouyoumjian and Pathak (1974)]) can be ascribed to the wavefronts.

The obtained reflected and diffracted fields are further used to determine the HF currents on the scatterer's surface. We note that these currents can be utilized for two purposes:

(i) as a basis to compute approximate scattered fields and cross-sections, or

(ii) as a basis to construct solutions using the High Frequency Integral Equation (HFIE) method which we discuss below.

The HFIE approach is based on an asymptotic form of the rigorous integral equations for surface currents, in which the "Ansatz" for the solution is represented as a superposition of ***known*** rapidly oscillating functions (corresponding to specific HF scattering processes) multiplied by ***unknown*** smooth functions varying slowly on the distance scale of the wavelength. We note that, in the past, several attempts of asymptotic integral-equation formulations have been reported, employing current representations as superpositions of products of rapidly and slowly oscillating functions, to describe two dimensional [Aberegg and Peterson (1995), Bruno, Sei, and Caponi (2002), Bruno (2002)], body of revolution [Altman, Mittra, Hashimoto and Michielssen (1996)], and some selected three-dimensional [Kwon, Burkholder and Pathak (2001), Mittra (2002)] scattering problems. In these approaches, the current Ansatz functions were constructed either analytically or numerically.

By discretizing the unknown smooth functions appearing in the Ansatz one arrives at a linear system of equations formally equivalent to that obtained in the MoM, but cor-

responding to basis functions defined on large, frequency independent supports. As a consequence, the number of unknowns is also frequency independent, in contrast to conventional MoM, in which the number of unknowns grows as $\sim L^2/\lambda^2$, where L is the scatterer size.

For realistically complex geometries, however,

(i) the Ansatz may have to include contributions from HF processes other than single and multiple reflections, in particular from single and multiple diffraction, and

(ii) because of the large number of reflection and diffraction processes the Ansatz construction becomes prohibitively complex.

We address both of the above problems. We construct appropriate forms of the Ansatz including diffraction contributions and verify their validity on a series of examples. We also formulate a numerical approach to the Ansatz construction based on computing approximate high frequency currents by means of the wavefront evolution method presented above. The numerical method of Ansatz construction leads in a natural way to the construction of large support basis functions and a subsequent Galerkin discretization of the high frequency integral equations.

2 The wavefront (WF) evolution method

2.1 Wavefront description

The wavefront (WF) evolution method may be considered an extension of the ray-tracing approach. Here, in addition to a set of propagating rays, we introduce a family of WF surfaces. Each of these surfaces is orthogonal to the rays, and is defined in terms of ray-ray connectivity, i.e., a surface mesh consisting of triangular faces whose vertices are points on the rays. This additional connectivity information allows a number of operations on the set of rays, which are difficult to implement in the conventional ray-tracing approach, where each ray (or small sets of rays, forming ray tubes) are treated separately. These manipulations include: (a) adding or removing rays, in order to maintain an approximately constant ray-ray distance when the wavefront expands or shrinks, (b) adding new rays at the shadow and reflection boundaries, (c) adding new rays generated by ***diffraction***. The last mechanism is the major new element we added in our development of the WF techniques. The work can be considered as the first attempt at incorporating diffraction in the WF evolution method.

We construct diffracted wavefronts by geometrical methods, and ascribe to them diffracted fields obtained from the Geometrical Theory of Diffraction (GTD) or Uniform Geometrical Theory of Diffraction (UTD) (see, e.g., [Keller (1962), Kouyoumjian and Pathak (1974)]).

In the present context the main purpose of using the WF methods is to determine the HF currents on the scatterer surface, either as approximate solutions to be used directly in computing the scattered fields, or as the elements of the Ansatz for the HF asymptotic solution. Correspondingly, we have devised a general procedure for computing the fields and currents on the scatterer surface, using field interpolation within "ray cells", i.e., triangular prisms built from triplets of adjacent rays, and the corresponding faces on the two consecutive WFs. We describe this method in Section 2.3.

Since the method will have to be applied to large and complex scatterers, our main concern is about the algorithm efficiency. In order to reduce the cost of computing the WF evolution, we plan to implement intelligent procedures of selecting only the needed portions of the WFs, and discarding the irrelevant ones. E.g., since in the considered problems we are interested not in the scattered far fields but only in the determination of the surface currents, we can eliminate those parts of the WFs which evolve in free space, without further interaction with the scatterer. As another extension of the present WF algorithm, we might allow for longer and perhaps variable WF evolution steps. We have already implemented an algorithm allowing several reflection processes within a single evolution step. It might be possible to similarly generalize the algorithm for generating diffracted WFs. In this case, the number of evolution steps, and thus the computational cost of the algorithm, could be significantly reduced. The overall number of evolution steps would be then dictated only by the considerations related to the tests of possible WF collisions with the scatterer, as discussed above (i.e., the unneeded parts of the WFs would be removed at the end of each evolution step).

As we mentioned above, the main use of the WF evolution method is to compute currents on the scatterer surface, either to be used directly to compute scattered fields, or to construct the HFIE solution Ansatz. In both cases, the number of the rays involved in the WF evolu-

tion should be of the order of the number of unknowns N needed to parameterize the smoothly varying functions in the solution (we recall that N is much smaller than the number of unknowns needed in the MoM formulation, and ***independent of the frequency***). Therefore, the total cost of the WF evolution algorithm is expected to be also proportional to N, multiplied by the relatively small number of evolution steps (also depending only on the scatterer geometry, and not on the frequency).

Below we discuss several aspects of our WF approach relevant in the present context.

2.2 Wavefront propagation and reflection

WF propagation in free space and WF reflection from scatterer surface are described according to the laws of Geometrical Optics (GO). Special care is taken in our algorithm to treat shadow and reflection boundaries with high accuracy. In particular, "ray tubes" represented by rays at the corners of a WF facet are split at these boundaries by creating new rays exactly at the boundary. This process is illustrated in Fig. 1 on an example of WF scattering on a flat screen.

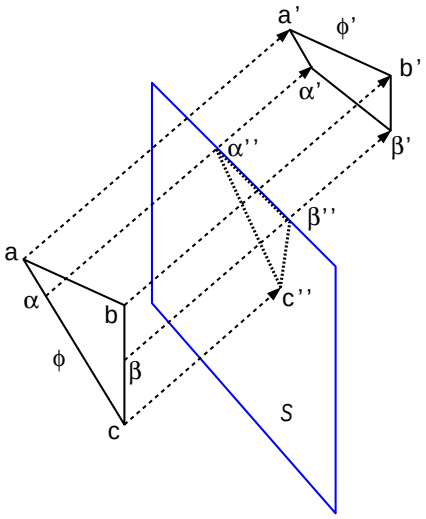

Figure 1 : Splitting of a ray tube into forward propagating and reflected parts.

Here the rays (a,a') and (b,b') (emerging from two corners of the WF facet (a,b,c)) pass without interacting with the screen. The third ray, (c,c''), hits the screen. The algorithm constructs two new rays, (α,α') and (β,β'), touching the edge of the screen at points α'' and β''. The original facet (a,b,c) is then split into a quadrilateral (a',b',β',α') (which is subsequently split into two triangles belonging to the evolved WF ϕ'), and a triangle (α'',β'',c''), which subsequently undergoes reflection.

The algorithm illustrated above can also be applied to reflection off smooth surfaces, and allows us to define the shadow and reflection boundaries with a high accuracy. For a scatterer surface of curvature radius R the error e in determining shadow and reflection boundaries is of the second order in the ray-ray spacing, $e = O(h^2/R)$.

2.3 Wavefront diffraction

Our algorithm for constructing WFs due to edge diffraction is based on the original GTD) [Keller (1962)], which in turn follows from the generalized Fermat's principle, and ultimately from the stationary-point asymptotics of the high-frequency scattering processes. We stress, however, that this statement applies only to the geometrical construction of diffracted WFs; the associated field amplitudes are computed using the better behaved Uniform Geometrical Theory of Diffraction (UTD) [Kouyoumjian and Pathak (1974), Pathak (1992)].

The main steps of the algorithm for construction of edge-diffracted WFs are as follows:

1. Identify those scatterer edges which may be sources of diffraction; these edges are referred to as "diffraction edges". In addition, create new rays (obtained by interpolation between pairs of rays on the WF) which exactly hit the diffraction edges; these are referred to as "diffraction source rays".

2. Generate sets of diffracted rays emanating from the diffraction edges, from the points hit by diffraction source rays.

3. Assign WF diffracted field values (obtained from UTD) and curvature parameters and the created diffracted rays.

4. Construct ray-ray connectivity (triangulation mesh) for the diffracted rays belonging to two consecutive sets (created by two consecutive diffraction source rays).

We discuss now the implementation of these steps.

Step 1 requires devising an algorithm for (1) detecting "sharp" edges, and (2) detecting the shadow boundary.

If the edge-diffraction algorithm is applied to a facetized scatterer surface, we assume that the "sharp edges" are sources of diffraction, while "smooth edges" have to the treated by a separate algorithm for smooth-surface diffraction.

The first algorithm can be applied directly to identify diffraction edges in wedges whose both faces are illuminated by the incident WF. Such tests for diffraction edges have to be generalized to wedges whose one face only is illuminated (Figs. 2 and 3).

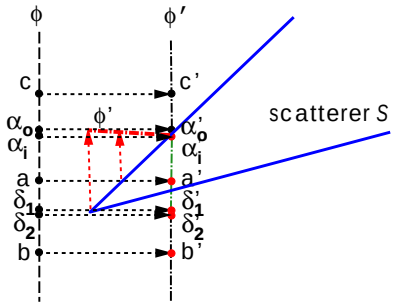

Figure 2 : Detection of a diffraction edge at the shadow boundary.

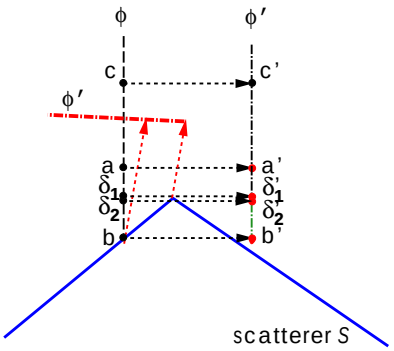

Figure 3 : Another case of a diffraction edge at the shadow boundary.

The second algorithm has to be extended to include a test for the normals to the scatterer surface intersected by the ray passing "just inside" the scatterer, as shown in detail in Figs. 4 and 5. This procedure is then able to detect a sharp edge at the shadow boundary.

An important element of the algorithm is that the identified "diffraction edges" are associated with and accessed through the WF mesh edges. As indicated in Fig. 6, the

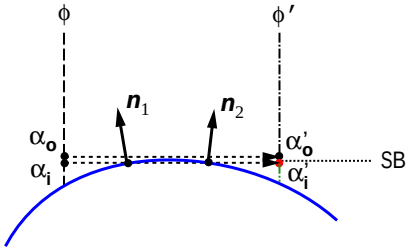

Figure 4 : Shadow boundary detection algorithm for a smooth scatterer surface.

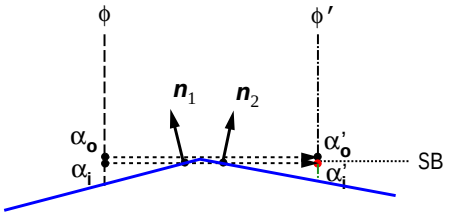

Figure 5 : The diffraction-edge detection algorithm for a scatterer surface with an edge at the shadow boundary. The edge is considered sharp or blunt depending on the angle between the face normals.

pairs of new rays $(\alpha_1, \alpha_2, \dots)$ hitting the sharp edge E emerge from the edges of the WF mesh $(e_1, e_2, \dots)$. Indeed, as illustrated in Figs. 2 and 3, these pairs of rays are created by interpolating rays at end vertices of the WF edges. For a facetized scatterer surface, also associated with the pairs of rays $\alpha_1, \alpha_2, \dots$ is the information on the surface facets intersected by the rays, and on the sharp edge itself (as the common edge shared by the two facets, as shown in Fig. 7).

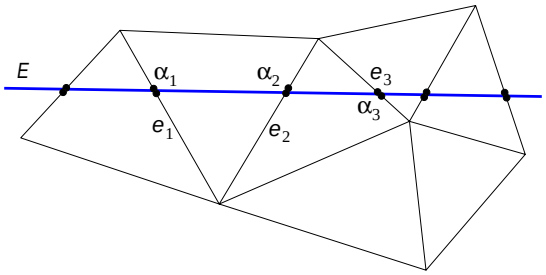

Figure 6 : Projection of the WF mesh on the view of the scatterer surface with a diffraction edge (denoted by E). Sets of pairs of new rays (marked by α_1, α_2, etc., are associated with edges if the WF mesh (e_1, e_2, etc.)

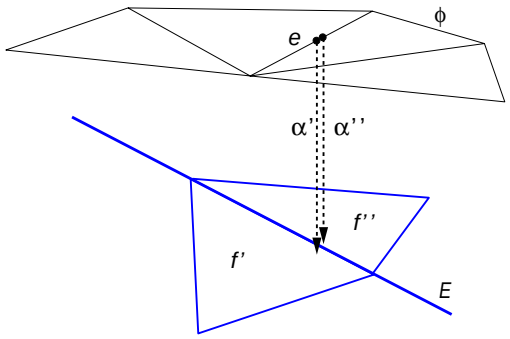

Figure 7 : A view of the facets f' and f'' of the scatterer surface intersected by the new rays (α' and α'') emerging from an edge e of the mesh on the WF ϕ.

Step 2 is performed in a loop through the edges e of the WF. From some of these edges there emerges a pair of new rays α, terminating at a diffraction edge. At the termination point we create a set of new rays (of length equal to the evolution step decreased by the length of the ray segments α), in the plane normal to the diffraction edge. The number of diffracted rays is fixed, and is determined on the basis of the required WF resolution (this element of the algorithm is not critical, since the number of rays will adjust itself during the subsequent evolution of the diffracted WF). This procedure is shown in Fig. 8.

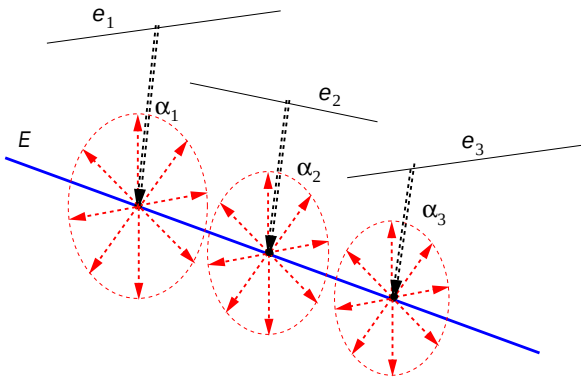

Figure 8 : Sets of diffracted rays emanating from the termination points of the ray segments α connecting WF edges and the diffraction edge.

Finally, **Step 3** is executed as a loop through the faces F of the WF. We consider here such faces F from two edges of which emerge pairs of new rays α (Fig. 9.) Through these rays we access two consecutive sets of diffracted rays, and create edges connecting the corresponding rays in the two sets, forming a surface consisting of quadrilateral facets. By triangulating that surface (Fig. 10), we arrive at a meshed diffracted WF.

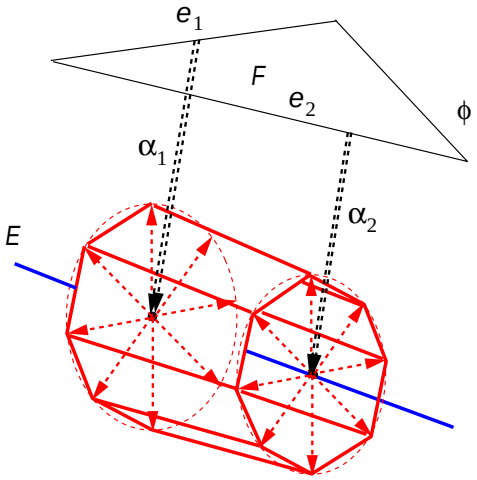

Figure 9 : Building connectivity for the diffracted rays.

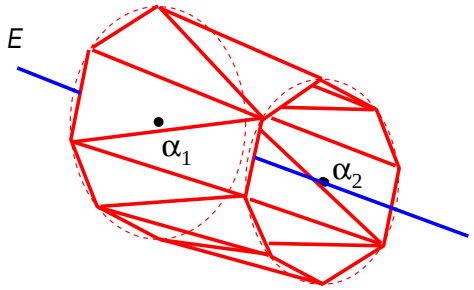

Figure 10 : Triangulation of the diffracted WF.

The algorithm does not currently handle corner diffraction (although such a generalization is certainly possible). In this situation, we modified the algorithm to avoid creating *spurious* diffracted rays associated with the edges. Specifically, we imposed the condition which prevents generating connectivity between groups of rays located on the two sides of the corner. This procedure will be illustrated in the examples presented below.

Further, although we constructed the diffraction algorithm for the case of triangulated scatterer surfaces, we do take into account the curvature of the diffraction edges (unless the edge forms a "sharp corner", according to some predefined specification). The approximate average curvature of the diffraction edge is computed on the

basis of several consecutive segments of the edges; this is a reliable procedure provided the lengths of the edge segments are small compared to the curvature radius.

We implemented the algorithm consisting of the steps 1–4 above, and tested it on the number of problems.

Example: Diffraction on a circular disc

As the first example we consider a circular disk with a plane WF incident on it in the normal direction. For definiteness, we place the disc at the origin of the reference system, in the (x,y) plane, and take the plane wave incident along the negative z-axis, with the electric field along the x-axis.

Figs. 11 and 12 show examples of the wavefronts after undergoing reflection and diffraction from the considered disc scatterer S. For clarity, only halves of the scatterer and the WF are shown.

In an early stage of development seen in Fig. 11 the WF consists of:

1. a flat segment (denoted "0") propagating downward, which has not interacted with the scatterer;
2. another flat segment (denoted "r1") propagating upward, and due to reflection off the scatterer; and
3. a toroidal surface (denoted "d1") around the edge of the disc, due to diffraction.

In a later development stage, shown in Fig. 12, the toroidal (diffracted) part of the WF has grown, and is intersecting itself. As expected, the color-coded field intensities are the highest near the upward and downward directions.

In the present case of a circular disc (diffraction on curved edges), the scattering amplitude and cross-section can be computed directly using the evolved WFs, since the fields behave asymptotically as spherical waves (with the $1/R$ dependence on the distance R). The far-field and the scattering amplitude can be then expressed in terms of the intensities of the fields on the WF, and the WF curvatures. The results for the bistatic cross-section agree very well with the standard GTD or UTD results. As expected, the main diffraction peak is not reproduced correctly by either GTD/UTD or WF approach, because of the caustic occurring in the back-scattering direction. Outside the peak, however, the agreement with the exact MoM computation is good, except for near-grazing angles, where multiple diffraction effects are expected to play a role.

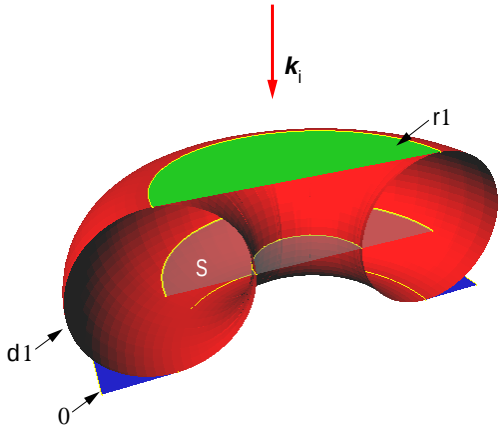

Figure 11 : One of evolution stages of the a plane WF incident on the disc (scatterer S), and undergoing reflection and diffraction. Colors show components of the WF due to individual processes: 0 for no interaction, r1 for single reflection, and d1 for single diffraction.

2.4 Computation of fields and surface currents

We describe now the application of WF evolution methods for obtaining fields associated with the WF, and the corresponding equivalent surface currents. As we discussed before, these currents can be used either *per se* as approximate HF solutions, or as the input for constructing the HF solution Ansatz (or, equivalently, the HF basis functions).

For a p.e.c. scatterer, the equivalent surface electric current is $\mathbf{J} = 2\,\hat{\mathbf{n}} \times \Delta\mathbf{H}$, where $\hat{\mathbf{n}}$ is the normal to the scatterer surface, and $\Delta\mathbf{H}$ is the magnetic field discontinuity across the scatterer surface.

One of the first questions we encounter when trying to determine surface currents is how these currents should be represented and parameterized. At high frequencies it is, clearly, impractical to use a representation of the current in terms of their values at selected points on the surface, since this would require about 10 sampling points per wavelength. A more useful representation is its parameterization as a sum of rapidly oscillating exponential factors multiplied by smoothly varying coefficients. Such parameterizations would be applicable in some surface patches D_j centered around some "current points" $\mathbf{R}_j$. The sizes of the regions D_j is assumed to be of the order of the local ray spacing, and they are required to cover the entire scatterer surface S.

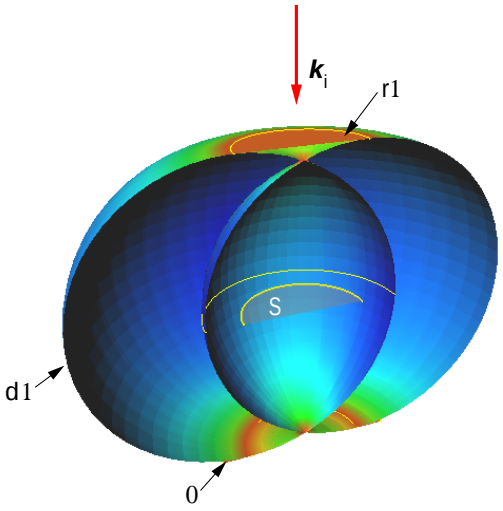

Figure 12 : A more advanced evolution stage of the WF shown in Fig. 11. Here colors indicate intensities of the electric field associated with the WF.

Let us assume for a moment that a set of M distinct rays (originating from different segments of the WF) coalesce at a current point $\mathbf{R}_j$. The conventional WF form of the fields suggest then the representation

$$\mathbf{J}(\mathbf{r}) = \sum_{m=1}^{M} \mathbf{A}_m(\mathbf{r})\, \mathrm{e}^{\mathrm{i}kS_m(\mathbf{r})} \qquad \text{for } \mathbf{r} \in D_j\,, \tag{1}$$

i.e., a sum of contributions of distinct rays arriving at $\mathbf{R}_j$. Here S_m's are the phases of the individual rays, defined so that $\nabla S_m(\mathbf{r}) = \mathbf{n}_m$, where $\mathbf{n}_m$ is the unit vector in the direction of the ray propagation. The amplitudes $\mathbf{A}_m$ are parameterized as constant amplitudes multiplied by the conventional ray divergence factors involving the ray evolution parameter and the curvatures. As we discuss later, the current representation (1) can be used as a parameterization of the solution (Ansatz) in the HFIE method.

Conceptually, the interpolation algorithm for calculating the fields can be stated as follows:

1. Specify a set R of "field points" $\mathbf{R}_j$ at which the fields are to be computed; the spacing of these points should be sufficiently small to resolve the variation of the amplitudes of the fields (but not variation of their phases).

2. At every step of the WF evolution find, for each "field point" $\mathbf{R}_j$, a set of nearby rays (within the distance of a few average ray-ray spacings). These rays are selected from the set of rays propagating from the previous WF to the current WF χ (Fig. 13).

3. For each of nearby rays ξ construct a ray $\xi_{\mathbf{R}_j}$ passing through the point $\mathbf{R}_j$ and parallel to the ray ξ. The length Δs of the ray is set to the distance between the point $\mathbf{R}_j$ and the WF, measured along the direction of the ray ξ.

4. By evolving the ray $\xi_{\mathbf{R}_j}$ forward in time find its intersection with the WF χ. Identify the WF face f intersected by the ray (Fig. 13). (We note that a continuation of the ray $\xi_{\mathbf{R}_j}$ may intersect further segments of the WF, but theses intersections are irrelevant, since we are only computing contributions of the rays evolved up to the WF χ.)

5. Identify the rays ξ_{f1}, ξ_{f2}, and ξ_{f3}, associated with the corners of the face f. Evolve these rays *backward* through the distance Δs to form an image f' of the face f. The prism built on the faces f and f' is our definition of the *ray cell*.

6. Check if the point $\mathbf{R}_j$ is located inside the face f'. If it is, continue to the point 7. If it is not, determine the average direction n_{123} of the rays ξ_{fi} $(i = 1,2,3)$, construct a ***new ray*** $\xi_{\mathbf{R}_j}$ emerging from $\mathbf{R}_j$ in the direction of n_{123}, and return to the point 4.

7. Interpolate field values associated with the ends of the rays ξ_{fi} to the point $\mathbf{R}_j$.

Several remarks and clarifications are in order here:

(a) The steps 3 to 7 are repeated for all rays passing near the observation point $\mathbf{R}_j$. If several near rays yield the same ray cell, only one of them is taken into account. Contributions to the fields from ***all distinct ray cells*** are added to the field representation at $\mathbf{R}_j$. The field is represented in analogy to Eq.(1), i.e., in the form of constant vector amplitudes and the corresponding wave vectors. Specifically, for each of the ray cells containing the point $\mathbf{R}_j$, we store the field amplitudes $\mathbf{E}_m(\mathbf{R}_j)$ and the phase $S_m(\mathbf{R}_j)$ evaluated at the observation point, as well as the gradient $\mathbf{n}_{j,m} = \nabla S_m(\mathbf{R}_j)$ at that point. These data provide a local parameterization of the field in the neighborhood of the point $\mathbf{R}_j$ as a sum of plane waves.

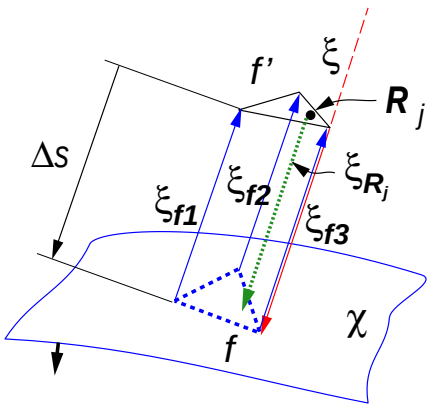

Figure 13 : The algorithm for computing a contribution of a ray to the fields at the observation point $\mathbf{R}_j$, by interpolating between rays ξ_{f1}, ξ_{f2}, and ξ_{f3} associated with a face f on the WF χ. The heavy arrow denotes the direction of WF propagation.

(b) If the observation points $\mathbf{R}_j$ are located on the scatterer's surface, it is understood that the WF χ is the WF computed as in the absence of the scatterer, i.e., before the effect of rays' reflections is taken into account. In fact, in our present implementation the WFs are first evolved without reflections, and then transformed by reflecting the rays.

(c) We note that our algorithm for field interpolation differs from the method being used in previous WF approaches, and based on a somewhat different concept of the "ray cell" [Vinje, Iversen, Astebol, and Gjöystdal (1996a), Vinje, Iversen, Astebol, and Gjöystdal (1996b)]. That concept of a ray cell requires using two consecutive WFs (the "previous" and the "current" ones), while our construction employs only one WF (the "current" WF). Our procedure was mainly motivated by applications to diffraction: in this case we may encounter a situation where the "previous" WF simply does not exist, because the current WF, due to a diffraction process, was newly created in the considered evolution step.

(d) In computing currents on an open surface we need to evaluate the magnetic field discontinuity, i.e., we have to compute fields at observation points slightly above and slightly below the surface. In this calculation we have to ascertain which side of the surface is illuminated by the given ray, and we have to take into account possible discontinuity of fields associated with the diffracted waves.

We also note that the above current computation algorithm is applicable both to GO WFs and to WFs including diffraction effects. It can be thus used both to generate GO currents as input for Physical Optics(PO)-type computations, and for creating the initial Ansatz (including diffraction) for the solution of the HFIEs. In particular, as we discuss in the following, the Ansatz can be represented precisely in the form of Eq.(1).

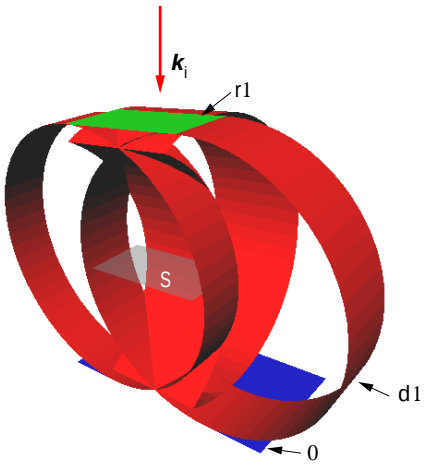

Figure 14 : A relatively early evolution stage for the a plane WF incident on the square plate (scatterer *S*). Colors show components of the WF due to individual processes: 0 for no interaction, r1 for single reflection, and d1 for single diffraction.

Example: Diffraction on a rectangular plate

For the previously discussed rectangular plate problem the relevant WFs, as computed by the present algorithm, consist of the incident wave and waves diffracted on the edges of the plate (Fig. 14 and 15). We note that the present algorithm generates disconnected segments of the WF associated with diffraction on the individual edges; in the full algorithm these segments would be connected by spherical WF due to corner diffraction.

To visualize the procedure of computing field and surface currents described above, we have generated graphical representations of the ray cells associated with the individual observation points.

Fig. 16 shows an example, taken from the actual computation, of a set of ray cells containing one of the observation points, in this case a point located slightly above the plate. As expected, there are five ray cells containing the observation point: one (*I*) due to the incident WF,

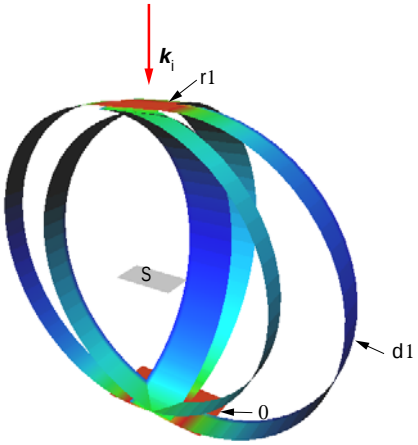

Figure 15 : A more advanced evolution stage of the WF shown in Fig. 14. Here colors indicate intensities of the electric field associated with the WF.

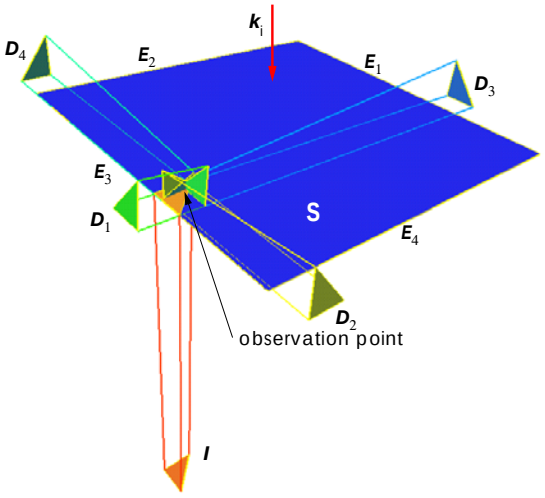

Figure 16 : Ray cells associated with an observation point slightly above the plate scatterer S, due to the incident wave (I), and waves diffracted on the four sides of the plate. The faces denoted by $D_1,\ldots,D_4$ are located on the four FWs emitted from the edges $E_1,\ldots,E_4$.

and four ($D_1,\ldots,D_4$) due to the diffracted WFs emerging from the four sides of the plate. For an observation point below the plate the cell due to the incident WF is absent.

An an example of an application of our procedure of current computation, we computed induced currents on a $10\lambda\times 10\lambda$ plate for a normally incident plane WF, and used them to evaluate the bi-static cross-section. In Fig. 17 we display a comparison between bi-static cross-sections for v-polarization, calculated with the (a) MoM method, (b) WF approach without edge diffraction contributions, and (c) WF approach with edge diffraction. It is seen that edge diffraction contributions to the current play an important role in improving the agreement of the WF result with the MoM computation (some discrepancies are expected, since corner diffraction and multiple diffraction effects are not taken into account in the WF algorithm).

3 HFIE approach

The approach is based on an asymptotic form of the rigorous integral equations for surface currents, in which the "Ansatz" for the solution is represented as a superposition of ***known*** rapidly oscillating functions multiplied by ***unknown*** smooth functions varying slowly on the distance scale of the wavelength.

As we discuss below, the method can be alternatively formulated as the MoM with suitably chosen basis functions of large, frequency-independent supports. Typically, these basis functions are (a) dependent on the incidence angle, (b) dependent on the geometry of the entire scatterer.

In the most basic case of a convex smooth scatterer the Ansatz can be realized simply as follows:

1. Take the PO current induced on the scatterer surface by the incident field as the rapidly oscillating function.

2. In the lit region, discretize the smoothly varying function with the resolution independent of the wavelength.

3. In the shadow boundary region (of width $\sim\sqrt{\lambda}$), discretize the smoothly varying function with the higher resolution, of the order of a fraction of λ.

It can be shown by means of the asymptotic analysis of the resulting integral equations that, in the considered case, the Ansatz described above is sufficient to correctly describe the solution in both the lit and the shadow region, with the accuracy better than any inverse power of the wavenumber $k=2\pi/\lambda$. One of the reasons why such a relatively simple Ansatz is possible is that the current

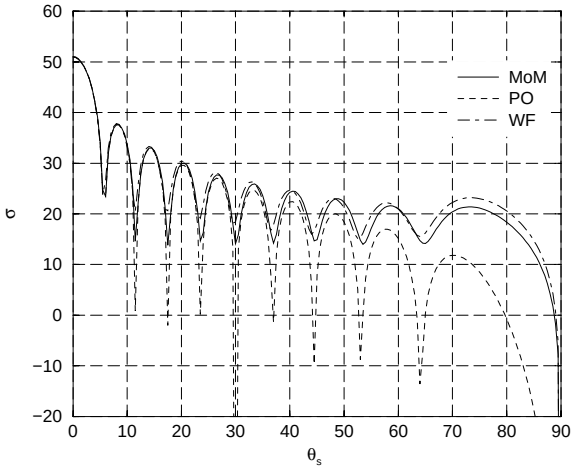

Figure 17 : Comparison between the bi-static cross-sections of a $10\lambda \times 10\lambda$ plate illuminated with a v-polarized normally incident wave calculated with the MoM method, the WF approach without edge diffraction contributions, and WF approach with edge diffraction contributions.

components due to diffraction on the smooth surface are damped ***exponentially*** away from the shadow boundary.

The situation is, however, more complex in the cases of non-convex and non-smooth scatterers.

First, on a concave scatterer, the incident wave may be reflected, according to the laws of geometrical optics (GO), a number of times. Hence, the leading (GO) term in the Ansatz will contain, in general, not only the incident wave, but also the reflected waves.

Secondly, in the presence of sharp edges the currents and the scattered fields contain in general diffraction contributions which do not decay exponentially with the distance from the diffraction source, but rather fall off according to a power law; for instance, diffraction on a straight wedge with flat faces generates currents and fields proportional to $1/\sqrt{kr}$, where r is the distance from the diffraction point. In this case it is impossible to incorporate the diffraction effects in the Ansatz by merely increasing the smooth-function discretization density near the diffraction source. Because of the slow, power-law decay of the diffraction contributions, the dense discretization region would have to extend through a distance controlled only by the scatterer geometry, and not the wavelength. The cost associated with this discretization would be then of the same order as the discretization cost of the MoM, and would defeat the purpose of using the Ansatz. Thus, the oscillatory behavior of the diffracted wave must be included in the Ansatz ***explicitly***.

Further, for a smooth, but ***concave***, scatterer explicit inclusion of diffracted wave contributions in the Ansatz may also be necessary. Such a situation may occur when a wave diffracted on a smooth part of the boundary illuminates another part of the scatterer. Then, although the surface currents due to the smooth-surface diffraction are localized near the shadow boundary, the diffracted wave may fall off according to the same $1/\sqrt{kr}$ law as for edge diffraction, and the currents induced by this wave on the scatterer surface will not be localized.

Moreover, even for smooth and ***convex*** scatterers, the spatial extent of the diffracted wave contribution near the shadow boundary may grow large, if the scatterer curvature becomes small. In fact, the exponential damping of the diffracted wave is controlled by the extinction length proportional to $R(\lambda/R)^{1/3}$, which may become quite large in realistic situations. In such cases the cost of the dense discretization may be too high, and it may be more advantageous to include the diffraction contribution explicitly in the Ansatz.

To summarize, one can identify the following elements of the HFIE approach:

- ***Construction of the Ansatz.*** It follows from the above discussion that, for arbitrarily shaped geometries, the HF solution Ansatz may have to explicitly include currents due not only to GO processes (multiple reflections), but also currents due to ***diffraction*** processes. In addition, contributions to the current due to any combination of a diffraction process with any number of GO reflection processes are as important as the contribution of the diffraction process itself.

  A new element in our construction of the solution Ansatz is the explicit inclusion of diffraction terms, whose form is derived from the asymptotic diffraction theory. In the present formulation we consider only objects built of flat surfaces, and therefore we include edge diffraction only. In more general problems involving curved surface diffraction, it will be necessary to supplement the Ansatz with additional terms containing suitable exponential factors with complex wave vectors. Examples of such terms are discussed in [Altman, Mittra, Hashimoto and

Michielssen (1996), Kwon, Burkholder and Pathak (2001)] in the context of numerical methods of Ansatz construction.

One may also observe that, except for the simplest geometries, analytical construction of an Ansatz including multiple reflection and diffraction contributions becomes a prohibitively complex task. Here, the wavefront evolution approach, discussed in Section 2, renders itself as a natural numerical tool for providing the fast oscillating Ansatz terms due to surface currents created by distinct rays.

- ***Discretization and construction of the impedance matrix.*** The impedance matrix is constructed according to the Galerkin method. The matrix is expected to be partly sparse, due to the suppression of matrix elements involving highly oscillatory integrands, and the dominance of stationary-point contributions. It is possible to predict which matrix elements will be negligible, and thus reduce the storage and computational time requirements.

- ***Matrix compression.*** For large problems (in the sense of a large number of the "HF unknowns", independent of the wavelength) it will be necessary to develop matrix compression methods.

- ***Solution procedure.*** The linear system arising from the discretization will be solved by means of an iterative, minimum-residual type, method, using fast matrix-vector multiplication associated with the matrix compression.

We describe below the main elements of the approach.

3.1 Discretization and basis functions

The general idea of the HFIE method is to represent surface currents on the scatterer as linear combinations of ***known*** rapidly oscillating functions (associated with the incident, reflected, or diffracted waves), and ***unknown*** smooth functions.

Here we propose a specific implementation of this idea, in the spirit of the Galerkin method. We start with partitioning the object surface S into patches, say, Π_α, of sizes that may be large compared to the wavelength λ, and, asymptotically, independent of λ. The only exception from this rule would occur in some small regions (such as the vicinity of the shadow boundary on a smooth surface). In these regions a denser discretization is required, and thus the patches will be smaller (down to the size of the fraction of λ).

We then parameterize the current $\mathbf{J}(\mathbf{r})$ as

$$\mathbf{J}(\mathbf{r}) = \sum_{\alpha} \sum_{m=1}^{M(\alpha)} j_{\alpha m} \mathbf{\Psi}_{\alpha m}(\mathbf{r}) \tag{2}$$

where the basis functions $\mathbf{\Psi}$ are supported on the patches Π_α. To every patch Π_α there correspond $M(\alpha)$ basis functions, each including a different oscillatory function. The basis functions $\mathbf{\Psi}$ depend, in general, on the incident wave.

As follows from the representation (2), the sizes and distribution of the patches should be such as to ensure that the expected variation of the smooth functions is correctly reproduced. Thus on large smooth areas of the scatterer the patches Π_α will be large, while in regions rich in geometrical detail the patch sizes will have to be controlled by the size of the details and the resulting variation of the solution (the rapid variation of the solution in this case is unrelated to the wavelength).

Various ways of constructing the basis functions $\mathbf{\Psi}_{\alpha m}$ are possible:

- A simple parameterization of $\mathbf{\Psi}_{\alpha m}$, for each m, would be a product of a "relatively smooth" function $\mathbf{\Phi}_\alpha(\mathbf{r})$ and an exponential $\exp(\mathrm{i}\mathbf{k}_{\alpha m}\cdot\mathbf{r})$. Here the functions $\mathbf{\Phi}_\alpha$ might be, say, piecewise linear (rooftop-type), to ensure a reasonable continuity of the solution in the absence of the oscillatory factors. In the exponentials the wave vectors $\mathbf{k}_{\alpha m}$ are those of the appropriate incident, reflected, or diffracted waves illuminating the patch Π_α (hence, in general, they depend on α).

- The functions $\mathbf{\Phi}_\alpha$ could be made more smooth (perhaps C^∞), and could be constructed according to the "partition of unity" concept (such that their sum would be equal to unity). In this case the patches Π_α would partly overlap. This modification would reduce (to exponentially small) sizes of the matrix elements that are already small due to rapid oscillations of the functions $\mathbf{\Psi}$ (as we discuss below).

- The functions $\mathbf{\Phi}_\alpha$ might include non-oscillatory, but rapid variation of the solution, such as the behavior of currents near the boundaries of a surface. Such

factors would automatically arise from the diffraction terms in the approximate HF solutions (obtained from UTD). An alternative possibility would be to use a denser discretization (smaller patches) in the regions of rapid non-oscillatory variation of the solution.

- The use of a quadratic, rather than linear, phase factor might be appropriate, in situations where the rapidly oscillating factor in the solution deviates significantly from a plane waves e.g., in the vicinity of a diffraction source, or near a reflection point on a strongly curved surface.

The number $M(\alpha)$ of basis functions associated with the given patch will depend on the geometry, on the incident wave, and on the required accuracy. In principle, all nonzero contributions of reflected waves should be kept along with the incident wave, since they are of the same order in $1/k$. Terms due to diffraction should be included hierarchically, depending on the diffraction type and order (with edge diffraction suppressed by $1/\sqrt{k}$, tip diffraction suppressed by $1/k$, etc.). Also, combinations of a given diffraction process and reflection are, again in principle, equally important as the diffraction alone.

A practical method of constructing the basis functions $\mathbf{\Psi}_{\alpha m}$ would be as follows:

1. Partition the object into patches Π_α, and select smooth "characteristic functions" χ_α of the patches.

2. Using wavefront (WF) evolution or sufficiently advanced ray tracing methods, combined with UTD, compute approximate asymptotic current $\mathbf{J}^{\text{as}}$ on the object. More precisely, for every patch Π_α and for every segment m of the WF incident on the patch, find the smooth amplitude $\mathbf{A}_{\alpha m}$ of the current, and the wave vector $\mathbf{k}_{\alpha m}$ (or, more generally, parameters of the quadratic approximation to the WF). Using UTD takes care of possible discontinuities of the current at shadow boundaries, but does not eliminate infinities due to caustics. It is an open question how to best handle these. However, we should remember that we are concerned here only with finding the correct rapidly varying functions. The smooth coefficients multiplying these functions do not have to be accurate; they will be corrected by solving the integral equations.

3. Construct the basis functions as

$$\mathbf{\Psi}_{\alpha m}(\mathbf{r}) = \chi_\alpha(\mathbf{r})\, \mathbf{A}_{\alpha m}(\mathbf{r})\, e^{i\mathbf{k}_{\alpha m}\cdot\mathbf{r}}. \tag{3}$$

Before solving the HFIEs, or even computing the matrix elements, we can easily test the validity of the constructed Ansatz in cases where an exact solution $\mathbf{J}_{\text{ex}}(\mathbf{r})$ to the scattering problem is available (it can be obtained, e.g., from a rigorous MoM computation). The test consists in verifying how well the known solution can be approximated by using the set of HF basis functions of Eq.(2). In other words we can compute the error of the least-squares approximation

$$\mathbf{J}_{\text{ex}}(\mathbf{r}) \simeq \sum_\alpha \sum_{m=1}^{M(\alpha)} j_{\alpha m} \mathbf{\Psi}_{\alpha m}(\mathbf{r}). \tag{4}$$

The least-squares problem is defined by minimizing the error

$$E = \int \mathrm{d}r \left| \mathbf{J}_{\text{ex}}(\mathbf{r}) - \sum_\alpha \sum_{m=1}^{M(\alpha)} j_{\alpha m} \mathbf{\Psi}_{\alpha m}(\mathbf{r}) \right|^2, \tag{5}$$

which leads to the linear system of equations

$$\sum_{\beta n} \left(\mathbf{\Psi}^*_{\alpha m}, \mathbf{\Psi}_{\beta n} \right) j_{\beta n} = \left(\mathbf{\Psi}^*_{\alpha m}, \mathbf{J}_{\text{ex}} \right). \tag{6}$$

Alternatively, we can simply solve the over-determined system

$$\sum_\alpha \sum_{m=1}^{M(\alpha)} \mathbf{\Psi}_{\alpha m}(\mathbf{r})\, j_{\alpha m} = \mathbf{J}_{\text{ex}}(\mathbf{r}) \quad \text{for } \mathbf{r} \in \text{discretization set} \tag{7}$$

by performing the QR factorization of the rectangular matrix involved. In any case, having determined the solution j, we substitute the solution elements $j_{\alpha m}$ back into Eq.(5), and thus find the error E.

3.2 Solution procedure

Having defined the basis functions $\mathbf{\Psi}_{\alpha m}$, we can proceed as in the conventional Galerkin method with the number of unknowns equal to

$$N_{\text{HF}} = \sum_\alpha M(\alpha). \tag{8}$$

The matrix elements are then given simply by

$$A_{\alpha m,\, \beta n} = \int \mathrm{d}r_1\, \mathrm{d}r_2\, \mathbf{\Psi}^*_{\alpha m}(\mathbf{r}_1)\, G(\mathbf{r}_1 - \mathbf{r}_2)\, \mathbf{\Psi}_{\beta n}(\mathbf{r}_2) \tag{9}$$

where G is the Green function. (The complex conjugation in applying $\mathbf{\Psi}$ as testing functions is essential, as discussed below.)

A straightforward computation of the matrix elements (9) may be nontrivial and expensive, considering the rapidly oscillating factors in the basis functions. This problem requires further investigation, also in connection with the partial sparsity of the matrix, and possible compression methods.

3.3 Properties of matrix elements

As we just mentioned, the factors in the integrands defining matrix elements (9) are rapidly oscillating, and therefore many of the matrix elements will be small, or will receive contributions only from limited regions (stationary points).

We note that, in general, there may even be a continuum of stationary points for a given integral. As an example, we consider a one-dimensional current distribution depending on the coordinate x, and take both the basis functions $\mathbf{\Psi}_{\alpha m}$ and $\mathbf{\Psi}_{\beta n}$ proportional to $\exp(\mathrm{i}kx)$. In this case the integral

$$\int \mathrm{d}x_1\,\mathrm{d}x_2\,\mathbf{\Psi}^*_{\alpha m}(x_1)\,G(x_1-x_2)\,\mathbf{\Psi}_{\beta n}(x_2) \tag{10}$$

leads to the expression

$$\int \mathrm{d}x_1\,\mathrm{d}x_2\,\mathrm{e}^{-\mathrm{i}kx_1}\,\mathrm{e}^{\mathrm{i}k|x_1-x_2|}\,\mathrm{e}^{\mathrm{i}kx_2}\cdot(\text{smooth functions})\,, \tag{11}$$

which receives large contributions from the region $x_1 > x_2$; this region of integration corresponds to the basis function $\mathbf{\Psi}_{\alpha m}$ located to the right of $\mathbf{\Psi}_{\beta n}$, i.e., to $x_\alpha > x_\beta$, where x_α and x_β are centers of the supports of the basis functions.

This example also shows why it is essential to complex-conjugate the testing basis functions: without complex conjugation we would not be able to construct any large matrix element (such as Eq. (10)), unless in the set of considered basis functions $\mathbf{\Psi}$ there would be a basis function proportional to $\exp(-\mathrm{i}kx)$, and this is by no means guaranteed. In other words, the original (not conjugate) basis functions $\mathbf{\Psi}$ are not good testing functions for the same set of trial functions $\mathbf{\Psi}$.

In general, many integrals defining matrix elements will have no stationary points, and will be therefore small, leading to a ***sparse*** matrix A. The degree of suppression of such matrix elements will depend on the properties of the smooth functions appearing in the basis functions. In particular, if these functions are in the class C^∞, the small matrix elements are exponentially small, i.e., smaller than any inverse power of k.

On the other hand, as we have seen in the one-dimensional example mentioned above, contributions to the matrix elements may come not only from isolated stationary points, but from continuous extended regions. For this reason, we cannot, in general, expect the impedance matrix to be entirely sparse (i.e., to have only a finite number of elements per row or columns, for the growing matrix size).

In any case, however, having a parameterization of basis functions such as Eq.(3), it is relatively easy to predict which matrix elements will be negligibly small, and create only the nonzero part of the matrix.

3.4 Compression of the impedance matrix

While partial matrix sparsity is helpful, it will not be sufficient to handle many large realistic problems, for which even the ***reduced*** number of HF unknowns, N_{HF}, may be of the order of tens of thousand, or more. Therefore, impedance matrix compression will be necessary, and development of a new compression scheme will be required, since none of the known compression techniques is applicable here.

A possible approach is to use plane-wave representations of currents and fields, such as those underlying FMM. In this context, we have initiated developing a version of FMM, which might be called a "sparse FMM".

In the conventional FMM the fields radiated by the given distributions of currents are parameterized in terms of signature function, i.e., distributions of fields at quadrature points on the unit sphere, representing directions of the emitted field. For surface problems, the number of these quadrature points is of the order of the number of the current elements in the original current distribution, counting about 10 current elements per wavelength. Therefore, the cost of constructing, storing, and using such signature functions in unacceptably high in the high-frequency asymptotics.

On the other hand, in the high-frequency limit, the radiated field distributions are expected to be strongly collimated about the directions related to the directions of the

wave vectors $\mathbf{k}_{\alpha m}$ appearing in the basis functions such as in Eq.(3) (in practice, many basis functions may share the same wave vector). It might be thus possible to parameterize the signature functions in a more economical way just by specifying the field distributions in the narrow cones about the wave vectors' directions. The required number of parameters would then not exceed $O(N_{\rm HF})$, where $N_{\rm HF}$ is the number of the HF unknowns (Eq.(8)). In this sense, we build a "sparse" HF representation of the signature function.

Further, in computing interactions between distant clusters, the fields associated with given wave-vector directions will propagate only if the directions match. This criterion corresponds to the stationary-point criteria in the computation of matrix elements.

Several problems remain to be analyzed and solved: for example, an efficient algorithm for converting between the current representation (2) and the signature functions, and an efficient parameterization and computation of translation operators. In view of these uncertainties, the development of HFIE matrix compression should be considered highly innovative, but also high-risk.

4 Validity tests of the HFIE Ansatz for currents; multiple reflection, diffraction, and surface wave contributions

In order to provide more information on the feasibility of the proposed HFIE solution scheme and to verify its ability of capturing effects associated with **diffraction** and **surface waves**, we have carried out several numerical validations for suitably selected non-trivial scattering problems involving a square plate, a strip, a dihedral, and a trihedral.

The results of our analysis, presented in the following two sections, demonstrate that it is possible to construct sufficiently simple and numerically efficient representations of currents in the form of a HF Ansatz which would accurately capture diffraction and surface wave contributions at a significantly lower cost than the corresponding Method of Moments approaches (with matrix compression enhancements). In all calculations we use an Ansatz given as a superposition of terms associated with single, double, and multiple reflections, and edge-diffracted wave contributions.

4.1 Least-squares computations with an analytical Ansatz

As the first example, we analyze the HF Ansatz construction for a plate illuminated by a plane wave (Fig. 18). We take into account only the lowest order ($1/\sqrt{k}$) diffraction effects, i.e., only first-order edge diffraction.

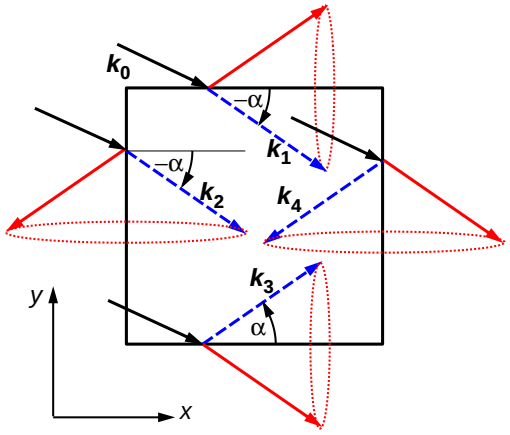

Figure 18 : A plate, with indicated projection $\mathbf{k}_0$ of the incident wave vector $\mathbf{k}_{\rm i}$ on the plate plane, and the "diffraction cones" generated on the four edges of the plate. The wave vectors associated with the waves diffracted from sides 1, 2, 3, 4 of the plate are denoted by $\mathbf{k}_1$ to $\mathbf{k}_4$.

In this approximation the Ansatz will consist of (a) the directly incident wave, and (b) four diffracted waves originating from the four sides of the plate.

In this case the HF basis functions $\mathbf{\Psi}_{\alpha m}(\mathbf{r})$ associated with a given surface patch Π_α are

$$\mathbf{\Psi}_{\alpha m}(\mathbf{r}) = \chi_\alpha(\mathbf{r})\,\hat{\mathbf{p}}_m\,e^{i\mathbf{k}_m\cdot\mathbf{r}}\,, \quad (m=0,1,2,3,4)\,. \tag{12}$$

The term $m=0$ is due to the incident wave, and $\mathbf{k}_0$ is the projection of the incident wave vector $\mathbf{k}_{\rm i}$ on the plate. The remaining four components are due to waves diffracted on the four edges of the plate. Each of the wave vectors $\mathbf{k}_m$ has length $|\mathbf{k}_m| = |\mathbf{k}_{\rm i}|$ ($m=1,2,3,4$), and lies on the intersection of the plate with the relevant diffraction cone associated with the plate side m. The angle α marked in Fig. 13 is the angle between the incident wave vector $\mathbf{k}_{\rm i}$ (***not*** its projection $\mathbf{k}_0$), and the upper edge of the plate (parallel to the x-axis in Fig. 18). Finally, the polarization vectors $\hat{\mathbf{p}}_m$ ($m=0,1,2,3,4$) are unit vectors defining the direction of the electric current. They are

determined from the condition that the electric current is related to the magnetic field jump $\Delta\mathbf{H}$ across the scatterer surface by $\mathbf{J} = \hat{\mathbf{n}} \times \Delta\mathbf{H}$, where $\hat{\mathbf{n}}$ is the normal to the surface. Hence, denoting by $\hat{\mathbf{h}}_m$ the direction of the magnetic field associated with the m-th wave vector $\mathbf{k}_m$, we have

$$\hat{\mathbf{p}}_m = \hat{\mathbf{n}} \times \hat{\mathbf{h}}_m \,. \tag{13}$$

For an arbitrary illumination angle, the diffracted waves (contained within the diffraction cones associated with the respective edges) will illuminate only parts of the plate. We could incorporate those conditions in the Ansatz by setting to zero the basis functions located in the shadow region. In our computation, however, we use the full sets of HF basis functions for all patches, expecting that the corresponding coefficients resulting from the solution of the equations will be practically zero in the shadow region. This option has the advantage of being simpler (although computationally somewhat more expensive), and allowing a smooth transition for the current at the relevant shadow boundaries (thus potentially reducing the approximation error).

We applied the Ansatz constructed above to scattering on a square, $10\lambda \times 10\lambda$ and $20\lambda \times 20\lambda$, perfectly conducting plates, and on a $20\lambda \times 4\lambda$ perfectly conducting strip. For definiteness, we align the geometries with the (x,y) coordinate system, and take the electric field of the incident wave along the y-axis.

We have carried out a numerical verification of the proposed Ansatz, by performing a least-squares fit of the ***known*** currents (obtained from the accurate MoM solution) as linear combinations of the basis functions (12). According to procedure described above, we divided the plate into rectangular patches, assigned to them the basis functions listed above, and solved the least-squares problem directly by QR factorization.

Representative results for the surface current on the $10\lambda \times 10\lambda$ square plate in the case of a normally incident plane wave are shown in Fig. 19. The plate was divided into 10×10 patches of unequal sizes, allowing for a denser discretization near the edges of the plate; effectively, the interior of the plate was discretized with only 4×4 patches. The exact currents and currents obtained using the Ansatz form of the solution are almost identical.

However, a more detailed error analysis shows that the error due to the approximation of the exact current with

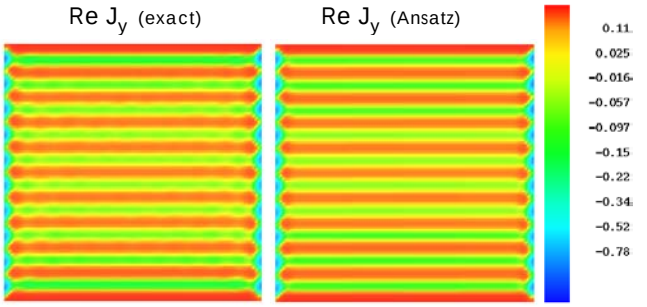

Figure 19 : Comparison of the exact current and the approximate current of Eq.(4) in the case of a normally incident plane wave.

the linear combination (4) comes almost entirely from the edges of the plate, i.e., from the regions where the current is singular (due to the "edge behavior" $\sim 1/\sqrt{x}$, where x is the distance from the edge). This result suggests that the accuracy of the expansion (4) can be further improved by taking the edge behavior into account when constructing the HF basis functions.

In Fig. 20 we compare the bi-static cross-sections for the vertical polarization, obtained from the exact (i.e., MoM) and the Ansatz solutions, again for the $10\lambda \times 10\lambda$ plate, discretized with $N_{\mathrm{LF}} = 29{,}800$ MoM unknowns. The least-squares fit to the current with five HF basis functions on each of $10 \times 10 = 100$ rectangular patches required $N_{\mathrm{HF}} = 500$ unknowns. For comparison, we also present the PO solution. It is seen that the full Ansatz is able to reproduce the exact result almost ideally, while the PO solution shows large deviations near 90°.

In Fig. 21 we compare back scattering cross-sections for the vertical polarization computed using the exact current, the full Ansatz current, and the PO approximation. For comparison, we also present a fit with only one basis function per patch, corresponding to the incident wave, included in the Ansatz (using the same number of N_{HF} unknowns). It is seen that while the full Ansatz is able to reproduce the exact result almost ideally, the limited Ansatz gives a result deteriorating at angles closer to 90°, and the PO approximation starts to deviate significantly from the correct result already at relatively small angles.

The cross-sections in Fig. 21 suggest a typical behavior associated with ***surface waves*** – a significant enhancement of the actual cross-section, compared to the PO approximation, at about 10° to 20° off the grazing inci-

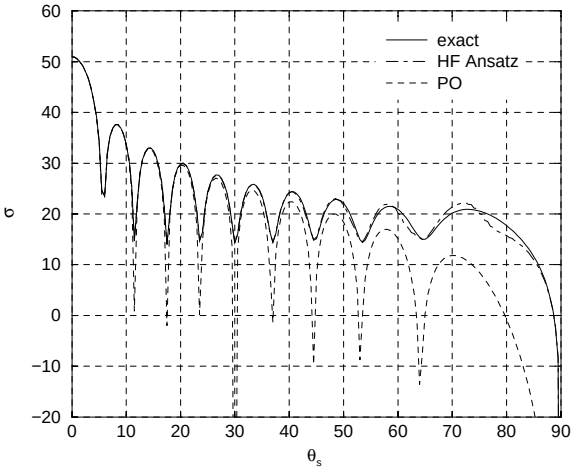

Figure 20 : Comparison of the bi-static cross-sections for the exact and approximate currents for a plate illuminated with a normally incident plane wave.

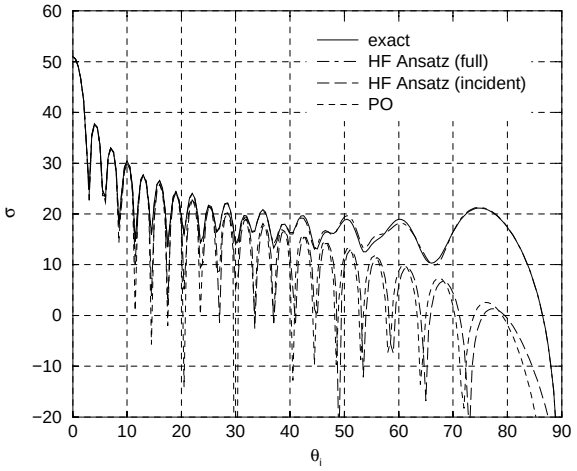

Figure 21 : Comparison of the back-scattering cross-sections for the plate using the exact current, approximate currents obtained with the full Ansatz and the Ansatz with the incident wave only, and the PO current.

dence. As a more prominent case exhibiting the surface-wave behavior, we analyzed, as the second example, a $20\lambda \times 4\lambda$ strip. The results for the exact and approximate cross-sections, analogous to Fig. 21, are shown in Fig. 22. Again, the exact cross-section is reproduced very well by the full Ansatz (including the incident wave and diffracted waves). On the other hand, neither a single-term Ansatz associated with the incident wave, nor the PO solution, were able to reproduce the exact cross-section.

Results of Fig. 22 indicate that the full HF Ansatz is able to accurately describe the current behavior giving rise to surface waves. We emphasize that the Ansatz parameterization is highly economical: the considered case requires $N_{\mathrm{LF}} = 23,760$ unknowns for the LF MoM solution, and 8,241 current sampling points (i.e., 16,482 current variables); at the same time, the full Ansatz is specified by means of HF basis functions on only 10×4 patches, giving rise to the total of $N_{\mathrm{HF}} = 200$ unknowns (the strip HF discretization is also shown in Fig. 22).

As a further illustration of the behavior of the HF currents we show below, in Figs. 23 and 24, results of the MoM computation of currents for a larger plate, of size $20\lambda \times 20\lambda$, for the incident wave at the 45° elevation angle, with the wave vector in the (x,z) plane, and with the electric field along the y axis. It is evident that the features of these current distributions can be reproduced by an Ansatz involving the incident and diffracted waves, with the wave vectors indicated in the figures.

As the subsequent example of the proposed HF solution Ansatz, we consider scattering on a dihedral consisting of two $10\lambda \times 10\lambda$, perfectly conducting plates. The purpose of this calculation is to demonstrate the HFIE method's ability to capture accurately ***multiple scattering and cross-polarization effects***.

In this case there are 19 terms in the Ansatz for a single quadrilateral patch. These terms represent plane wave contributions associated with single reflection, double reflection, single diffraction, and reflection-diffraction terms. Again we find that the HFIE Ansatz (involving a rather nontrivial interplay of various multiple scattering and diffraction terms) is able to reproduce very accurately the numerically exact MoM predictions, including cross polarization effects.

Fig. 25 shows the dihedral geometry, and the rigorous MoM results for hh and vh back-scattering cross-sections, which indicate the large size, in some angular ranges, of the cross-polarized (vh) term. The Ansatz least-squares fits were computed for a set of selected incidence angles. The results for the currents are shown in Figs. 26 and 27, and the cross-sections for these cases agree with the MoM result within about 1 dB.

It can be seen that the Ansatz we have chosen is able to reproduce a rather nontrivial behavior of the current (Figs. 26 and 27). In particular, the z-component of the

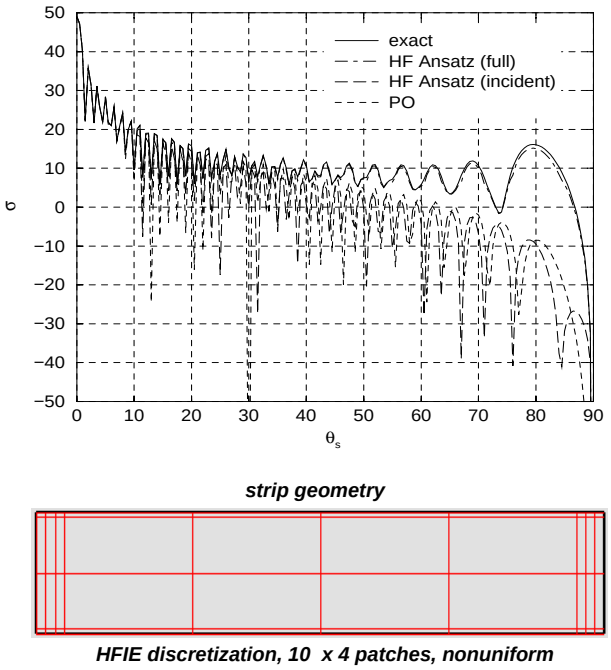

Figure 22 : Comparison of the back-scattering v-polarization cross-sections for a perfectly conducting $20\lambda \times 4\lambda$ strip. Partition of the strip into patches for the HFIE computation is also shown.

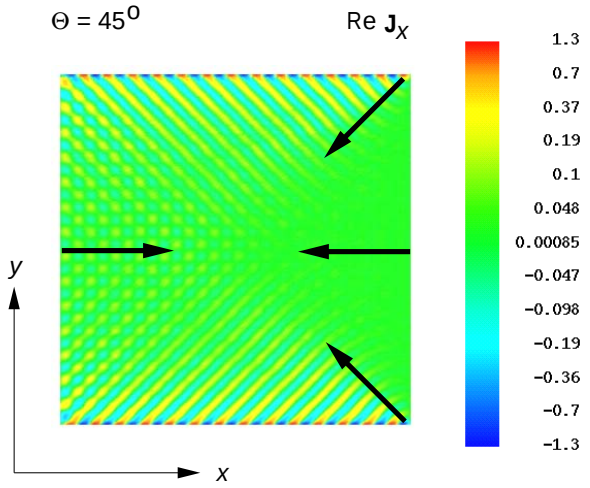

Figure 23 : The distribution of the x-component of the current for incidence at 45°. The arrows indicate the wave vectors appearing in the Ansatz, due to edge diffraction.

current (see Fig. 27), which strongly contributes to the cross-polarization term in the cross section, is very well reproduced by the Ansatz despite the fact that its magnitude is significantly smaller than that of the y-component.

4.2 Approximate computations with a numerical Ansatz

As the final example we consider scattering on a trihedral (Fig. 28). Our calculations for the trihedral apply to the case of the interior illuminated by a plane wave of wave vector $\mathbf{k}_i$. In a generic configuration, and to the first order in diffraction processes, each of the three faces is illuminated by:

1. The incident wave.
2. The geometrical reflections of the incident wave from the other face(s); these are either singly or doubly reflected waves.
3. Diffracted waves due to the ***incident wave*** illuminating any of the nine edges present in the problem.
4. Diffracted waves due to any of the ***reflected waves*** illuminating any of the nine edges.
5. Geometrical reflections of any of the diffracted waves generated in processes 3. and 4.

We stress that contributions from all combinations of geometrical reflections accompanying diffraction should be included in the Ansatz, since, as we discussed before, they are of the same order as diffraction itself.

Construction of the explicit expression for all the basis functions appearing in the Ansatz for the trihedral geometry constitutes already a relatively complex task. There are close to a hundred of basis functions for each face of the trihedral, and they have complicated dependencies on the incident wave vector (just to mention the fact that, in general, only parts of the faces are illuminated by the incident wave reflected from other faces; or the fact that, generally, the diffracted waves illuminate also only parts of the faces, and waves reflected from these faces illuminate even more complex regions of other faces).

We think that a practical method of determining the complete set of basis functions would be a numerical one, based on the construction of a relevant set of WFs. In the considered approximation the WFs will be due only to reflections and to single edge diffraction. From the information contained in the WFs and the associated fields

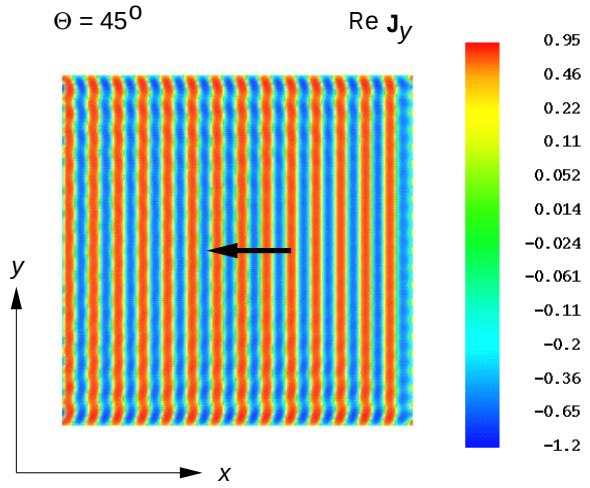

Figure 24 : The distribution of the *y*-component of the current for incidence at 45°. The heavy arrow shows the direction of the incident wave vector projection.

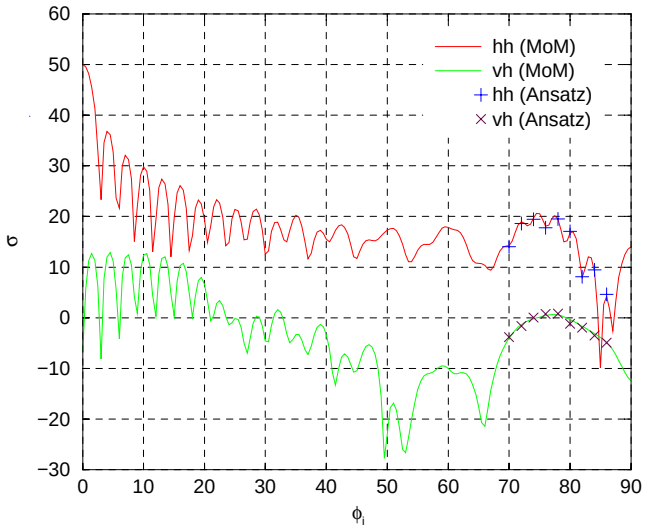

dihedral geometry, HFIE discretization, 2 x 9 x 9 patches, nonuniform

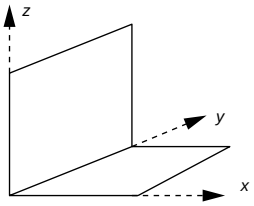

Figure 25 : Backscattering cross-section for a dihedral consisting of two $10\lambda \times 10\lambda$ perfectly conducting plates for hh and vh (cross-polarization). The curves show the exact (MoM) results, the points show the Ansatz least-squares fits.

(computed using UTD), we would determine the amplitudes and wave vectors associated with the basis functions defined on the individual patches of the surface.

In the meantime, however, in order to verify, at least approximately, the relative importance of terms associated with different physical processes which contribute to the Ansatz, we carried out a comparison of (a) our "zero-th" order HFIE code version (described below), and (b) our rigorous LF code with matrix compression.

The preliminary zero-th order version of the HFIE method constructs the Ansatz based only on Geometrical Optics (GO). In this approach the scatterer surface is triangulated and the solution is represented in the form of Eq.(2), with the HF basis functions of the type of Eq.(3),

$$\mathbf{\Psi}_{\alpha m}(\mathbf{r}) = \chi_\alpha(\mathbf{r})\,\mathbf{A}_{\alpha m}\,e^{i\mathbf{k}_{\alpha m}\cdot\mathbf{r}}, \qquad (14)$$

with constant amplitudes $\mathbf{A}_{\alpha m}$. This representation is constructed by accumulating contributions of all the rays (incident or reflected) illuminating the given patch α, and the index m refers to GO reflection order of the ray. The coefficients $j_{\alpha m}$ in Eq.(2), as well as the amplitudes $\mathbf{A}_{\alpha m}$ and the wave vectors $\mathbf{k}_{\alpha m}$, are determined from the polarization and the incidence angles of the ray incident on the patch; these parameters, in turn, are computed from the GO laws governing the behavior of the rays. In the present zero-th order version of the HFIE method diffraction contributions were not yet included. (The results obtained with the zero-th order version of the HFIE method are similar to what could have been obtained with ray shooting and bouncing methods.)

In simple terms, the main difference between the fully developed, planned version of the HFIE method and its zeroth-order version is that, while both algorithms use the similar form and the identical number of terms in the Ansatz, the coefficients $j_{\alpha m}$ in Eq.(2) differ: While in the case of the full HFIE method these coefficients need to be determined by solving a suitable system of linear equations, in the case of the zero-th order version of HFIE they are to have the values following from the PO prescription for a plane wave associated with a multiply reflected ray incident on a given triangular facet. Another difference is that in the full implementation the Ansatz would include additional terms due to diffraction, calculated, e.g., using the Physical Theory of Diffraction

(PTD) [Ufimtsev (1971)].

In order to assess, at least approximately, the relative importance of terms associated with different physical processes which contribute to the Ansatz, we carried out a comparison of (a) our zero-th order HFIE code version, and (b) our rigorous LF code with matrix compression. The results are presented in Figs. 28 – 30. In Fig. 28 we display surface current distribution for 10 GHz plane wave illumination. In Figs. 29 and 30 we display comparisons between the mono-static cross-sections computed with our HF research code module for the trihedral geometry at 30 and 90 GHz with and without the multiple scattering contributions. In both cases the incident wave was horizontally polarized, and incident at $\theta_i = 80^\circ$.

The results of our analysis for the trihedral at several frequencies, demonstrate that the inclusion of ***multiple scattering*** terms is critical for obtaining a satisfactory agreement of the HFIE predictions with the numerically exact LF method. The calculations employing only the single-scattering HF method (being equivalent to the conventional PO method) are simply inadequate. The full calculations, on the other hand, give us confidence in the ability of the HFIE method of capturing the key physics of the interactions of EM waves with geometries leading to significant multi-bounce signatures.

We note that zero-th order HFIE code without diffraction terms reproduces relatively well the qualitative and quantitative features of the angular distribution of the mono-static cross-section predicted by the rigorous LF calculations at 30 GHz. (For comparison, in the same graph we display the conventional single-scattering (equivalent to physical optics solution) whose failure, in this case, is evident.) The calculations (requiring 900,201 unknowns) confirm the trend of the angular pattern and give us confidence that our HFIE approach reproduces the qualitative features of the exact calculations relatively well.

We have also carried out HF calculations for the mono-static cross-section for a trihedral at 90 GHz. We have not performed, at this moment, the comparison with the results of a LF MoM code with matrix compression. The calculation would require about 10,000,000 unknowns.

To summarize, our preliminary numerical experiments indicate that the Ansatz provided by the approximate zero-th order version of the HFIE method is capable of successfully capturing the leading multiple scattering effects which dominate the corner reflector RCS.

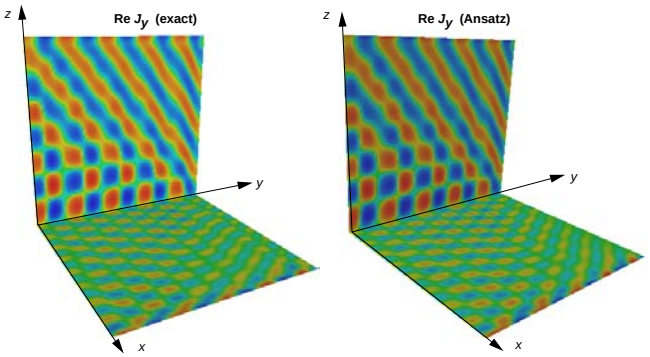

Figure 26 : Distribution of the *y*-component of the current on a dihedral consisting of two $10\lambda \times 10\lambda$ perfectly conducting plates for a horizontally polarized plane wave incident at the angles $\theta = 70^\circ$ and $\phi = 30^\circ$.

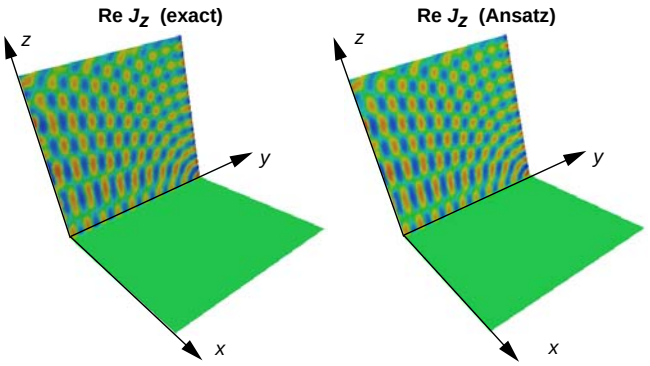

Figure 27 : Distribution of the *z*-component of the current on a dihedral consisting of two $10\lambda \times 10\lambda$ perfectly conducting plates, for the same incident wave angles $\theta = 80^\circ$ and $\phi = 80^\circ$.

5 Computational cost estimates

The essence of the HF methods is that their computational cost should be independent of the wavelength, and should be only a function of the scatterer geometry. The complexity estimate of the HFIE method is similar to that of the MoM (with matrix compression), but with the dramatically reduced number of unknowns, N_{HF}, ***independent of the frequency***.

The "geometrical" HF methods used to generate the solution Ansatz are expected to scale as $O(N_{\mathrm{HF}})$. The cost (per iteration) of the iterative solution of the HFIEs themselves ranges from $O(N_{\mathrm{HF}}^2)$ with no compression and no (geometry-dependent) matrix sparseness, to the expected complexity $O(N_{\mathrm{HF}} \log N_{\mathrm{HF}})$ with compression.

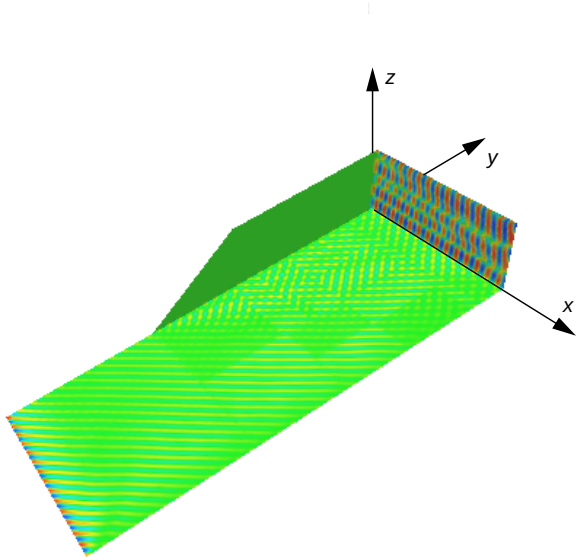

Figure 28 : Trihedral geometry used the calculations. We also show distribution of one of the current components for 10 GHz plane wave illumination.

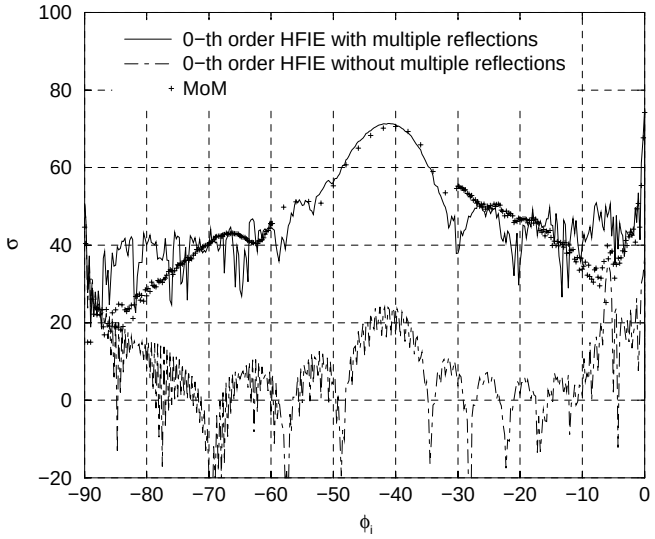

Figure 29 : Mono-static cross-sections at 30 GHz for the trihedral, computed with the zeroth-order HFIE code with and without multiple reflection contributions. Diffraction terms were not included yet. Results of the exact LF MoM calculation (requiring 900,201 unknowns) are represented with cross symbols.

These estimates should be compared with the cost of the iterative LF solution, which, with matrix compression, is $O(N_{\rm LF}\log N_{\rm LF})$ per iteration, and the relevant number of unknowns scales as $N_{\rm LF}\sim(L/\lambda)^2$, where L is the scatterer size.

There remains, however, the question of the number of HF unknowns, $N_{\rm HF}$, which, although frequency-independent, remains strongly dependent on the scatterer geometry. We recall that a simple procedure for constructing the HF basis functions is to specify patches on the scatterer's surface (of sizes independent on the frequency), and construct (by interpolation) all rays passing through a selected "observation point" on the patch. Each of these rays provides then an approximate local plane-wave contribution to the field, and to the current, on the patch. Therefore, the number of basis functions associated with a given patch is equal to the number of distinct rays passing through the observation point on the patch. These rays include the ray due to the incident wave as well as to reflected and diffracted rays.

For complex geometries the number of such (multiply) reflected and (possibly multiply) diffracted rays may grow rapidly with the geometry complexity. It is, therefore, necessary, to formulate criteria according to which only the relevant rays will be selected.

A simple criterion can be based on introducing a threshold to eliminate rays and basis functions considered unimportant. With this prescription we use a ray-tracing or a wavefront algorithm to generate a possibly large number of rays incident at the observation point, due to various reflection and diffraction processes. For each ray we compute the (approximate) field value, i.e., the amplitude appearing in the plane-wave representation for the ray. We then select only those rays for which the amplitudes are larger than a certain fraction of the maximum amplitude.

The above prescription supposes that the approximate fields obtained from the HF solution are reasonable approximations to the actual fields, computed eventually by solving the integral equations for the currents. In some cases this presumption may not hold, and more insight into the properties of the expected solutions may be needed.

By using selection criteria such as the above, we expect to be able to achieve a reasonable balance between the accuracy and the computational cost of the solution. We expect that the hierarchy of the approximations will approximately reflect the asymptotic HF expansion, the simplest approximation being the zero-th order Geometrical Op-

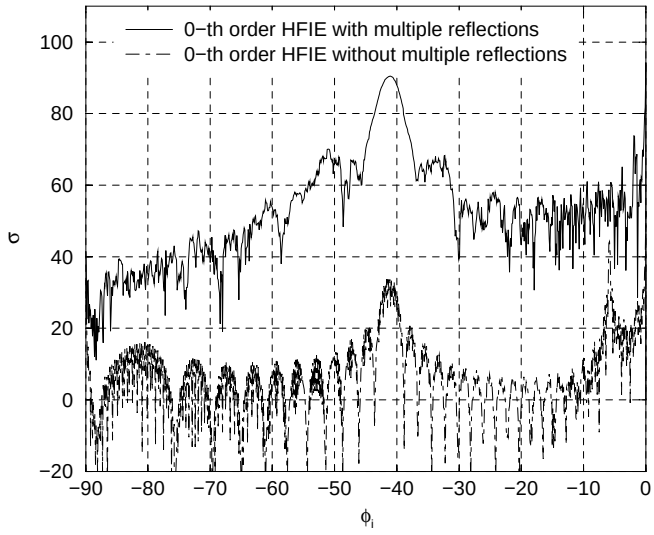

Figure 30 : Mono-static cross-sections at 90 GHz for the trihedral, computed with the HF module with and without multiple reflection contributions. Diffraction terms were not included yet.

tics, with the consecutive approximations corresponding to increasing orders of diffraction contributions.

6 Summary

We described key elements of two new approaches applicable to electromagnetic scattering at high frequencies: (a) wavefront propagation method and (b) high frequency integral equation approach. While both methods are based on quite different formulations, they share two common desirable features. Their complexity is ***frequency independent*** and the required object discretization is determined not by the wavelength but by the geometrical complexity of the scatterer.

Our discussion of the wavefront evolution technique, focussed mainly on the essential features of its practical implementation associated with the computation and interpolation of fields, which provide definite advantages compared to the conventional ray-tracing approach. Two new elements of the wavefront method were addressed in detail: (i) construction of the edge diffraction contributions, and (ii) procedure for constructing field and currents on the scatterer surface.

As for the HFIE approach, the main emphasis of our presentation was the construction of the solution Ansatz, and verification of its validity for several representative problems sensitive to such nontrivial phenomena as multiple reflections, diffraction, surface waves, and cross-polarization effects. While the form of the Ansatz is relatively straightforward for simple geometries, it becomes quite complicated for complex objects. We have described a general numerical procedure for the Ansatz construction, in which we determine the rapidly oscillating components of the Ansatz from fields generated by a sequence of wavefronts corresponding to physically relevant multiple reflection and diffraction processes.

The results we presented in the context of our discussion of the HFIE method demonstrate that it is possible to construct sufficiently simple and numerically efficient representations of currents in the form of a HF Ansatz which accurately capture diffraction and surface wave contributions at a significantly lower cost than the corresponding Method of Moments approaches (with matrix compression enhancements).

Finally, we note that both approaches considered here are in an early development stage and they will require substantial effort before they can be used to solve engineering problems of practical interest.

Acknowledgement: This work is partially supported by the AFOSR contract F49620-01-C-0045 and the US ARL contract DAAD17-02-C-0041.

References

Aberegg, K. R.; Peterson, A. F. (1995): Application of the integral equation asymptotic phase method to two-dimensional scattering, *IEEE Transations on Antennas and Propagation*, Vol. 43, pp. 534-537.

Altman, Z.; Mittra, R.; Hashimoto, O.; Michielssen, E. (1996): Efficient of representation of induced currents on large scatterers using the generalized pencil of function method formulation for large PEC scattering problems *IEEE Transations on Antennas and Propagation*, Vol. 44, pp. 51-57.

Bleszynski, E.; Bleszynski, M.; Jaroszewicz, T. (1996): AIM: Adaptive Integral Method for solving large-scale electromagnetic scattering and radiation problems, *Radio Science*, Vol. 31, pp. 1225-1251.

Bruno, O. P.; Kunyansky, L. E. (2001): Surface scattering in 3-D: an accelerated high order solver, *J. Comput. Phys.*, Vol. 169, pp. 80-110.

Bruno, O. P.; Sei, A.; Caponi, M. (2002): High-

order high-frequency solution for rough surface scattering problems, to appear in *Radio Science*.

Bruno, O. P. (2002): New high-order, high-frequency methods in computational electromagnetism, presented at the ARL CEM Workshop, Adelphi, MD, June 27-28 2002.

Cheng, L. J.; Kang, M.; Osher, S.; Shim, H.; Tsai, Y. (2004): Reflection in a Level Set Framework for Geometric Optics, *CMES: Computer Modeling in Engineering & Sciences*, vol. 5, no. 4, pp. 347-360.

Coifman, R.; Rokhlin, V.; Wandzura, S. (1993): The Fast Multipole Method for the Wave Equation: A Pedestrian Prescription, *IEEE Antennas and Propagation Magazine*, Vol. 35, pp. 7-12.

Keller, J. B. (1957): Diffraction by an aperture, *J. Appl. Phys.*, Vol. 28, pp. 426-444.

Keller, J. B. (1962): Geometrical theory of diffraction, *J. Opt. Soc. Am.*, Vol. 52, pp. 116-130.

Kouyoumjian, R. G.; Pathak, P. H. (1974): A uniform geometrical theory of diffraction for an edge in a perfectly conducting surface, *Proc. IEEE*, Vol. 62, pp. 1448-1461.

Kwon, D.; Burkholder, R. J.; Pathak, P. H. (2001): Efficient Method of Moments formulation for large PEC scattering problems using asymptotic phasefront extraction (APE), *IEEE Transations on Antennas and Propagation*, Vol. 49, pp. 583-590.

Mittra, R. (2002): Some novel techniques for efficient solution of large problems arising in compuational electromagnetics, presented at the ARL CEM Workshop, Adelphi, MD, June 27-28 2002.

Osher, S.; Fedkiw, R. P. (2002): The level set method and dynamic implicit surfaces, *Springer Verlag*, New York.

Pathak, P. H. (1992): High-Frequency Techniques for Antenna Analysis, *Proc. IEEE*, Vol. 80, 1, pp.44-65.

Ruuth, S. J.; Merriman, B.; Osher, S. (2000): A fixed grid method for capturing the motion of self-intersecting interfaces and related PDEs, *J. Comput. Phys.*, Vol. 163, pp. 1-21.

Steinhoff, J.; Fan, M.; Wang, L. (2000): A new Eulerian method for the computation of propagating short acoustic and electromagnetic pulses, *J. Comput. Phys.*, Vol. 157, pp. 683-706.

Ufimtsev, P. Y. (1971): Method of edge waves in the physical theory of diffraction, *Air Force Systems Command*, Document ID No. FTD-HC-23-251-71.

Vinje, V.; Iversen, E.; Gjöystdal, H. (1993): Traveltime and amplitude estimation using wavefront construction, *Geophysics*, Vol. 58, pp. 1157-1166.

Vinje, V.; Iversen, E.; Astebol, K.; Gjöystdal, H. (1996a): Estimation of multivalued arrivals in 3D models using wavefront construction - Part I, *Geophysical Prospecting*, Vol. 44, pp. 819-842.

Vinje, V.; Iversen, E.; Astebol, K.; Gjöystdal, H. (1996b): Estimation of multivalued arrivals in 3D models using wavefront construction - Part II, *Geophysical Prospecting*, Vol. 44, pp. 843-858.